Light-induced reflectivity transients in black-Si nanoneedles

P. Ščajev,[1,*] T. Malinauskas,[1] G. Seniutinas,[2,3] M. D. Arnold,[4] A. Gentle,[4] I. Aharonovich,[4]
G. Gervinskas,[2,3] P. Michaux,[2] J. S. Hartley,[2] E. L. H. Mayes,[5] P. R. Stoddart,[2] and S. Juodkazis[2,3,†]

[1]Institute of Applied Research, Vilnius University,
Saulėtekio Avenue 9, Bldg. III, LT-10222 Vilnius, Lithuania
[2]Faculty of Science, Engineering and Technology,
Swinburne University of Technology, Hawthorn, VIC 3122, Australia
[3]Melbourne Centre for Nanofabrication, ANFF, 151 Wellington Road, Clayton, VIC 3168, Australia
[4] School of Physics and Advanced Materials, University of Technology Sydney, 15 Broadway, Ultimo, NSW 2007, Australia
[5]School of Applied Sciences, RMIT University, GPO Box 2476 V, Melbourne, VIC 3001, Australia

(Dated: August 25, 2015)

The change in reflectivity of black-Si (b-Si) upon optical excitation was measured by the pump-probe technique using picosecond laser pulses at 532 (pump) and 1064 nm (probe) wavelengths. The specular reflection from the random pattern of plasma-etched b-Si nano-needles was dominated by the photo-excited free-carrier contribution to the reflectivity. The kinetics of the reflectivity were found to be consistent with surface structural and chemical analysis, performed by scanning and transmission electron microscopy, and spectroscopic ellipsometry. The surface recombination velocity on the b-Si needles was estimated to be $\sim 10^2$ cm/s . Metalization of b-Si led to much faster recombination and alteration of reflectivity. The reflectivity spectra of random b-Si surfaces with different needle lengths was modeled by a multi-step refractive index profile in the Drude formalism. The dip in the reflectivity spectra and the sign reversal in the differential reflectivity signal at certain b-Si needle sizes is explained by the model.

PACS numbers: 81.07.-b

I. INTRODUCTION

The fabrication and replication of nano-textured surfaces is a fast growing area of research, especially in the biomedical field where surface structures can have a significant effect on the functions of cells and membrane receptors[1]. When coated with thin films or nanoparticles of plasmonic metals, nanostructured surfaces are also widely employed as substrates for surface-enhanced Raman scattering (SERS)[2,3]. In this context, black-Si (b-Si) has attracted increasing attention, as the surface area, aspect ratio of the nano-needles, surface hydrophobicity, changes in the surface recombination rate and antireflection properties are all very useful parameters for energy and sensing applications[2,4,5].

The surface structure and properties of b-Si can be controlled via the plasma- or chemical- etching conditions used in fabrication. Black-Si solar cells with high efficiency ($> 18\%$) have been achieved[6], even without an antireflection coating. The tapered needles create a gradual change in refractive index, which reduces the reflectivity of a step-like change in refractive index, as demonstrated in the case of glass[7] and in some naturally nanostructured surfaces[8]. The porosity of Si can also be controlled by electrochemical etching to change the refractive index and surface passivation[9]. Future solar cells with light harvesting efficiencies of over 90% and a Si thickness of just micrometers have been designed using slanted conical holes[10].

In all of these light harvesting and sensor applications, structural defects and chemical contamination on the surface of plasma- (or chemically-) etched surfaces have to be understood and controlled. This study explores the effect of plasma etching on light localization, absorption and thermal properties, using a picosecond pump-probe spectroscopy technique to investigate the photoinduced reflectivity of b-Si. Black-Si with different morphologies was prepared by plasma etching. The unperturbed reflectivity of random b-Si surfaces was modeled by a multi-step refractive index profile and matched to experimental ellipsometry data.

II. RESULTS

All of the samples in this study were made by the same plasma etching recipe, but with different etching times. Figure 1 shows SEM images of b-Si etched for 5 min (a,b) and 25 min (c,d). The separation between the b-Si needles followed a diffusional dependence on etching time, with an average separation of 388 ± 20 nm for 5 min and 842 ± 30 nm for 25 min etch times (Fig. 1). For Batch No. 1, the separation was ~ 300 nm and the pillars had a pyramidal shape of height ~ 500 nm. Batches 1-2 had comparable pillar heights[11], while Batch 3 has a pillar height of 4 μm as evident from Fig. 1(d).

Figure 1(e) shows the surface chemical composition and morphology of a sample from Batch No. 3. X-ray photo-electron spectroscopy (XPS) revealed no significant differences between samples from Batches 1-3. Surface contamination by fluorine and oxygen was present due to the mixture of SF_6 and O_2 used for plasma etching. The tips of the needles were crystalline silicon without any amorphization or distinct oxide layer. This is an

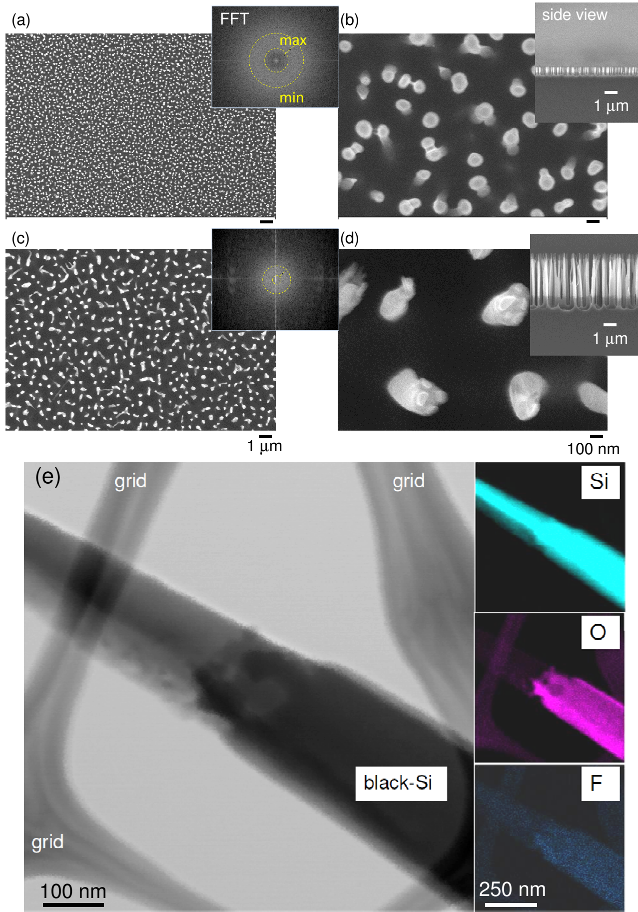

FIG. 1: Top view SEM images of b-Si etched for 5 min (a,b) and 25 min (c,d) (Batches 2 and 3, respectively). Insets in (a,c) are fast Fourier transform (FFT) images with the inner (max) and outer (min) dashed-circles corresponding to 692-261 nm (max-min) in (a) and 1635-573 nm in (c). Insets in (b,d) are side-view SEM images. (e) Elemental mapping was conducted using scanning-TEM mode and an EDS detector (Batch No. 3).

important point, as it allowed the optical response to be modeled without having to account for changes in surface composition.

The reflectivity of the samples was measured with a bifurcated optical fiber spectrometer, where white light illumination was delivered via the central fiber and the back-reflected (and scattered) light was collected by satellite fibers. As shown in Fig. 2, a recognizable reflectivity dip was observed and its spectral position and amplitude were dependent on the structure of the b-Si.

Although the reflection from the b-Si was low ($\sim 1-2\%$), it was close to specular. In a pump-probe experiment, specular reflection is not expected when the wavelength of the pump laser is smaller than the spacing between the needles. However, the reflectivity measured by pump-probe at a distance tens-of-centimeters from the b-Si surface was comparable to that measured with

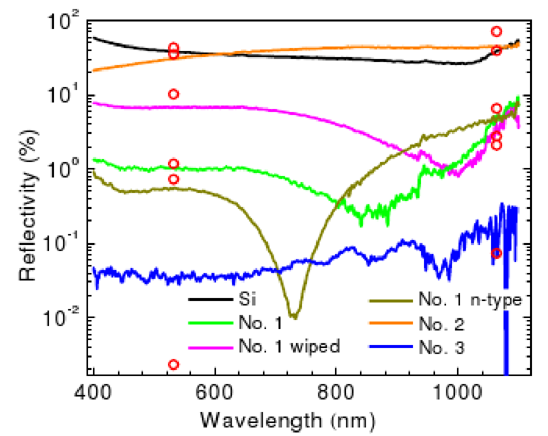

FIG. 2: Reflection spectra of different samples (see Experimental Section for details) measured at normal incidence by a bifurcated optical fiber spectrometer. The minima at 700-1000 nm correspond to reflection from a random structure of pillars ~ 0.5 μm high. The "wiped" sample indicates that the needles were mechanically abraded; the n-type b-Si was As-doped with $\langle 100 \rangle$ orientation and resistivity $R \leq 0.005$ Ω/cm made by the recipe of Batch No. 1. The Au coating was over 200 nm thick for the reflective mirror-like sample and was 50 nm for the least reflective Batch No. 3. The circles show the reflectivity measured by pump-probe experiments on the respective samples; the largest mismatch was for Batch No. 3.

the bifurcated fiber spectrometer directly at the surface. Hence, reflectivity (transmission) measurements can be carried out under laser illumination, providing a contactless optical measurement of excited carrier dynamics in the sub-surface regions of the needles.

The differential reflectivity, $DR(t)$, is defined in terms of the time-dependent sample reflectivity $R(t)$ and the equilibrium reflectivity R_0 (see Eq. 1)[12]. The differential reflectivity kinetics are dependent on the decay of the carrier density ΔN within a depth $d_{abs} \sim \lambda_{ex}/4\pi k_{ex} \simeq 2.1$ μm; here the excitation $\lambda_{ex} = 532$ nm and $k_{ex} \simeq 0.02$ are the pump wavelength and imaginary part of the refractive index of Si, respectively[13].

The longer wavelength probe is absorbed over a much longer distance, and thus the probe absorption is usually unimportant compared with the short scale refractive index changes due to interfaces and carrier profile. In b-Si the fraction of Si is reduced, making the effective depths longer[12,14]. The refractive index of Si for the probe beam is $n_{pr} = 3.5$ and $\omega_{pr} = 2\pi\nu_{pr}$ is the cyclic frequency of the probe. The backside of the b-Si samples was not polished, thus excluding any contribution of backside reflection to the measured DR signal (the scattered reflected light was blocked by an auxiliary aperture).

The proportionality factor n_{eh} represents the refractive index change per electron-hole pair in a unit volume. The Drude formalism[15] allows n_{eh} to be obtained according to Eq. 2, where the electron-hole mass in Si is $m_{eh} = 0.166 m_0$ and depends on the electron and hole

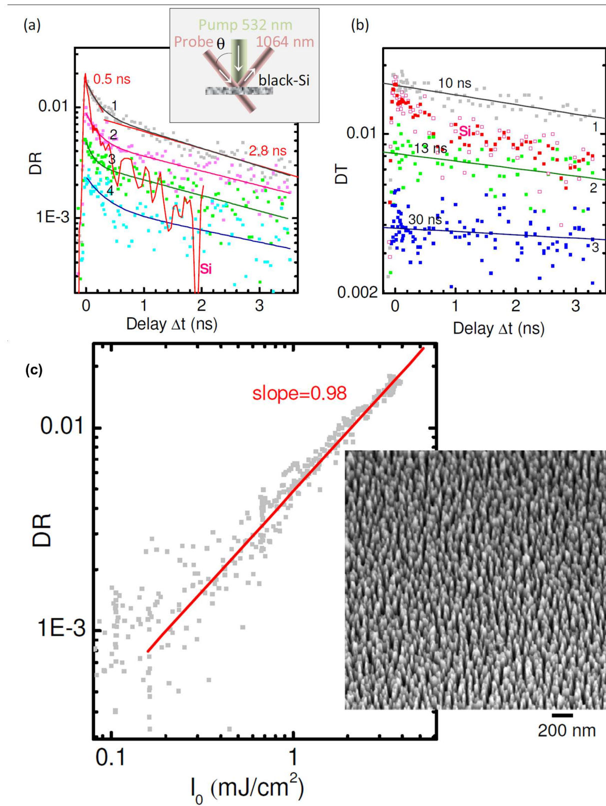

FIG. 3: Photo-induced changes of (a) reflection $DR = \Delta R/R$ and (b) transmission $DT = \Delta T/T$ for Batch No. 1 in a pump-probe experiment. Inset in (a): measurement geometry where the angle of incidence $\theta = 23^\circ$. Intensities in (a): 3.5 mJ/cm^2 *(1)*, 1.7 *(2)*, 0.9 *(3)*, 0.4 *(4)*, and in (b): 2 *(1)*, 1 *(2)*, 0.5 *(3)*. Si was measured as a reference (red markers) at 1.8 mJ/cm^2 excitation. The fitted (solid) curves are (a) bi-exponential and (b) single exponential fits. Note that the sign of DR for Si in (a) is reversed. (c) Power dependence of the reflection peak DR for Batch No. 1. The reflectivity of b-Si increased with excitation ($\Delta R > 0$) while it decreased ($\Delta R < 0$) for Si. Inset shows a slanted-view SEM image of the sample.

conductivity masses, $m_e = 0.26m_0$ and $m_h = 0.46m_0$[16], respectively, while ε_0 is the vacuum dielectric constant and m_0 is the electron mass[12]:

$$DR(t) = \frac{R(t) - R_0}{R_0} \approxeq -\frac{4}{n_{pr}^2 - 1} \left|n_{eh}\right| \Delta N(z = d_{obs}, t), \tag{1}$$

$$n_{eh} = -\frac{e^2}{2n_{pr}\varepsilon_0 m_{eh}^* \omega_{pr}^2}, \quad \frac{1}{m_{eh}^*} = \frac{1}{m_e^*} + \frac{1}{m_h^*}. \tag{2}$$

Note that n_{pr} is the refractive index for the probe beam, and $d_{obs} \sim \lambda_{pr}/4\pi n_{pr}$ is the effective probe observation depth at a single interface[12]. The factor n_{eh} was calculated as 9.3×10^{-22} cm^3 for Si. The differential transmission is defined as

$$DT(t) = \ln(T_0/T(t)) \approxeq \int_0^d \Delta\alpha_{pr}(t, z)dz, \tag{3}$$

where z is the depth coordinate. Note that these equations are applicable for bulk Si, while the absorption in the needles and reflection from the Si substrate must be considered for b-Si (for details see discussion later in this Section).

The refractive index changes due to free carriers $\Delta n_c = n_{eh}\Delta N$ are much higher than those due to temperature changes ΔT induced by excitation, $\Delta n_T = n_T \Delta T$, where $n_T = 2.2\times10^{-4}$ K^{-1} is the thermooptic coefficient of Si at room temperature[17]. The ratio $-\Delta n_c/\Delta n_T$ can be calculated according to $(n_{eh}/\hbar\omega_{ex})/(n_T/\rho C_p)$[18], where $C_p = 0.71$ J/gK is the heat capacity[19] and $\rho = 2.33$ g/cm^3 is the density of Si. The estimated ratio of ~ 19 indicates that refractive index changes due to sample heating by photo-excitation can be disregarded.

The time-dependent differential transmission of the probe beam (DT, Eq. 3) is obtained by integrating the excess carrier density over the sample thickness d at different delay times with respect to the pump beam[20]. Here T_0 and $T(t)$ are the transmission of the probe beam when the pump is off and on, respectively. The amplitude of DT is defined by the magnitude of the induced absorption change for the probe wavelength in Eq. 3, namely $\Delta\alpha_{pr}(t, z) = \Delta\alpha_{FCA} = \sigma_e\Delta n + \sigma_h\Delta p \sim \sigma_{eh}\Delta N$, which consists of the free carrier absorption coefficient $\Delta\alpha_{FCA}$ due to the excess concentration of electrons Δn and holes Δp, respectively; σ_e and σ_h are the absorption cross sections for the free electrons and holes, respectively, while σ_{eh} is the total free carrier absorption cross section[20] at concentration ΔN. The free carrier absorption modifies the imaginary part of the refractive index by[21] $\Delta k = \Delta\alpha_{pr}\lambda/4\pi$, which reduces to $\Delta k = \sigma_{eh}(\lambda)\Delta N\lambda/4\pi$. The dependence of Δk on wavelength λ can be approximated by[22] $\sigma_{eh}(\lambda) \sim (3.5 \pm 0.5) \times 10^{-18} \times (\lambda[\mu\text{m}])^{2.8}$ in the interval 0.86 - 2.0 μm. The peak DT signal is defined by the relationship $DT = \sigma_{eh}\Delta N_0/\alpha_{ex}$.

Batch 1 exhibited the best optical properties: the lowest surface recombination velocity, S, at the air-needle interface and the best absorption enhancement in Si i.e. the DR signal was 30% larger than in bulk Si. The darkest b-Si sample with the highest aspect ratio needles (Batch No. 3) showed no probe transmission after a 50 nm Pd coating, most probably due to large S and k - the imaginary part of the refractive index.

The reflection minimum at λ_{min}, observed in Fig. 2, can be explained by thin film interference between the top of the b-Si and the b-Si|Si interface. Thus reducing the needle length by mechanical abrasion shifted the minimum by 150 nm ("wiped" sample). A 200 nm Au coating provided very strong reflectivity, indicating that a reflective Au layer was formed over the tips of the densely packed needles (separation ~300 nm, see Fig. 1). In con-

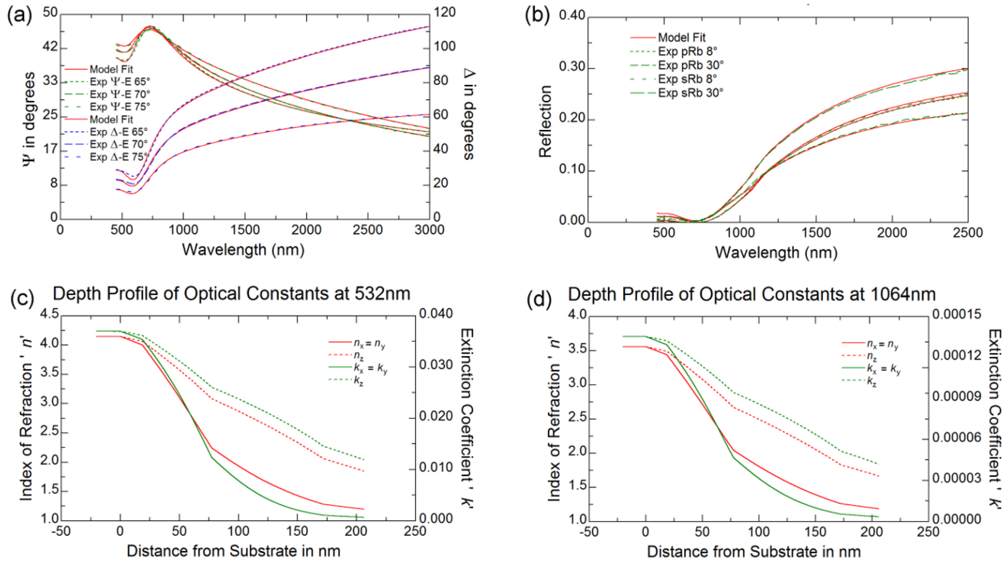

FIG. 4: Ellipsometry measurements and model results for a typical b-Si sample consisting of pyramidal needles. The reflectance ratio for the E-field of $s-$ and $p-$polarizations was measured as $\frac{r_p}{r_s} \equiv \tan(\Psi)e^{\imath\Delta}$ over a wide range of wavelengths, where $\tan\Psi$ is the reflection amplitude and Δ is the phase shift. (a) Ψ and Δ at different angles of incidence. (b) Simulated and experimental polarized reflectance spectra. (c,d) Geometrical depth profiles of refractive index $(n + \imath k)$ for which the best fit was achieved at 532 nm and 1064 nm, respectively.

trast, a strongly reduced reflectivity was observed for the 50 nm coating (Batch 3). This reduction may be related to the impact of long (~ 4 μm) and more separated ($\sim$800 nm) needles (Fig. 1d).

The DR decays in Fig. 3 are non-exponential and weakly excitation dependent, indicating that surface and nonlinear recombination may have an impact[14]. An upper bound of the surface recombination velocity in b-Si can be estimated, assuming that it occurs predominantly on the cylindrical needle surfaces. According to the relationship[23] $\tau_S = 0.282 d_n/S$, with needle diameter $d_n \sim 200$ nm and $\tau_S > 500$ ps, a surface recombination velocity of $S < 113$ cm/s was calculated on the needle surface. Such a low value is typical for Si passivated by native dielectric SiO_2[24]. A non-exponential decay may be caused by random variations in the d_n and S values. Therefore faster DR decays indicate larger S values. On metal-coated needles (Batch 2 in Fig. 3), the lifetime was found to be less than $\sim$10 ps, which leads to $S > 10^4$ cm/s, which is typical for Pd-metalised Si[25]. Note that noble metals such as Pt, Pd and Au are known to reduce the recombination lifetime in Si[26].

The DT decay rate (Fig. 3(b)) increases with increasing excitation intensity, indicating the presence of nonlinear recombination. The Auger coefficient in highly excited silicon is $C = 3 \times 10^{-31}$ cm^6/s in the 77 - 400 K temperature range[27]. The 1.8 mJ/cm^2 excitation provides $\Delta N_0 = 4.3 \times 10^{19}$ cm^{-3} and an Auger lifetime of $\tau_{Aug} = 3/(C\Delta N_0^2) = 6.7$ ns, which is close to the experimental results. Here, the factor of 3 accounts for an inhomogeneous distribution of excited carriers with depth[14]. The differential transmission peaks at $DT \simeq 0.018$ for 1.8 mJ/cm^2 excitation, according to $DT = \sigma_{eh}(1064\text{ nm})\Delta N_0/\alpha_{ex}$ and provided that $\sigma_{eh}(1064\text{ nm}) \simeq 3.7 \times 10^{-18}$ cm^2, which is close to the 4.2×10^{-18} cm^2 reported in the literature[22]. It is noteworthy that DT also probes the underlying Si layer as the excitation depth exceeds the b-Si thickness (in b-Si the carrier density should be homogeneous with ΔN_0 as the Si needles fill only a small fraction, $\sim$10%, of the b-Si volume). Thus DR is more advantageous for b-Si studies than DT.

For comparison, the DR decay was measured in bare Si. The decay rate was faster in bare Si than in Batch No. 1, indicating that Si has a higher surface recombination velocity than a b-Si covered Si surface. The curve on bare Si showed $DR = 0.02$ at 3.5 mJ/cm^2 excitation. The measured value is a close match for the theoretical value of $DR = 0.025$ from Eq. 1. The power law of DR, shown in Fig. 3, follows a linear dependence on the pump intensity, indicating that the absorption is excitation independent.

The DR decays were measured at different temperatures in a nitrogen cell (see Supplementary Information). The decay amplitude becomes larger and the decay is faster at higher temperatures. A doubling of the decay amplitude in the range 300-500 K correlates well with an increase in the absorption coefficient from 8×10^3 cm^{-1} to 1.5×10^4 cm^{-1} over the same range[15]. This is expected as $DR \sim \Delta N \sim \alpha$. The reduction in the initial lifetime from 0.6 ns to 0.15 ns also contributes to the increased absorption coefficient, as it leads to a doubling of the

carrier density near the surface, which in turn provides a four-fold reduction in lifetime as $\tau_{Aug} \sim 1/\Delta N_0^2$. A density of $\Delta N_0 = 7.5 \times 10^{19}$ cm^{-3} at RT with an Auger coefficient[27] $C = 3 \times 10^{-31}$ cm^6/s provides a lifetime of 0.59 ns, which is consistent with our results. Additionally, at the highest temperatures (600 K) surface recombination may increase due to increased carrier thermal energy, which allows the carriers to overcome the surface trap energy barrier on the needle surfaces, and thus leads to a much faster decay tail at 600 K.

Both ellipsometric and polarised angular reflectance data was used to retrieve the geometrical profile of the random tapered structures via a spectrally wide best fit. Figure 4 shows the measured and modeled ellipsometry (a) and reflectance (b) results for a typical b-Si sample. The structure was modeled using a graded bi-axial Bruggerman effective medium model[28] using the WVASE ellipsometric modelling software. The tapering of the structure can be seen in Fig. 4(c,d) with the refractive index going from that of bulk silicon at the base and reducing as it reaches the peaks. In order to get a good fit to the reflectance data at the longer wavelengths below the silicon bandgap, a small amount of backside reflection (4%) was included in the model, consistent with a somewhat wider collection angle than other measurements. For the purposes of initial fitting the graded profile was fitted with 5 nodes, each with 10 steps interpolated between each node. Starting values for the b-Si profile were based on the SEM profile, i.e. needles on top of pyramids (Fig. 1).

The effect of sample parameters on the pump-probe differential reflectance was explored using a detailed thin-film model. Free-carrier material properties were coupled with the pump intensity profile in the effective-medium stack, with a maximum external pump of 3.5 mJ/cm^2 at 532 nm (see the Experimental Section for details). Similarly to Eqs. 1 and 2, this model predicts that a negative change in reflectance is possible and will be highest at long wavelengths due to a stronger free-carrier effect and increased absolute reflectance. However, unlike the earlier equations, the detailed model also predicts the possibility of a positive change in reflectance due to spectral shifts.

Representative results are presented in Fig. 5, for a linear conical profile, since this is the simplest graded profile and a reasonable first approximation to the observed structure. Overall, the results show that (for a fixed probe wavelength) the sign of the differential reflectance oscillates with black-Si thickness, in particular changing from negative at small thicknesses, to positive and then to negative again near a dip in absolute reflectance. There are two effects contributing to this response, both of them due to photocarriers reducing the refractive index. Reduced single-interface reflection, as predicted by Eq. 1, affects all samples and is the most important effect in bulk Si. In black Si layers, there is a superimposed reflection oscillation, which on photoexcitation is blue-shifted by reduced optical path length. This shifted oscillation provides a plausible explanation for the pump-probe results, since Batch 1 (p-type) had a reflection minimum at around 900 nm with positive differential reflectance at 1064 nm, whereas other samples with different minima had small or negative differential reflectance. More pinched graded profiles (broader bases and needle-like tips) stretch the differential oscillations to longer wavelengths and broaden the absolute reflection dips for a given total thickness, which may refine the quantitative match to the experimental results, however the fundamental behavior remains the same.

In addition, the effect of the doping concentration was found to be minimal over practical resistivity ranges, assuming that backside reflection is ignored. Backside reflection can significantly alter the total reflectance, so we have carefully considered this assumption. Photoexcitation may change the material absorbance enough to switch the backside reflection on or off, even though the carriers are only concentrated within the pump absorption length (about 1 μm in depth). At 1064 nm and 3.5 mJ/cm^2, the effect is negligible below 0.002 Ω.cm, and has largely saturated by about 0.2 Ω.cm, in line with the change in mobility. For bulk Si samples where the frontside reflection is very high, the effect is only about 2% of the differential signal, but for low reflecting samples with sufficient resistivity the effect could be an important contributor. However, it is reasonable to ignore backside reflection here because the rough backside surface scatters this contribution and it is largely excluded by the specular collection employed. This is confirmed by the observed pump-probe intensity dependence, which is linear in contrast to the non-linear backside dependence. The low resistivity used in Fig. 5 would suppress backside reflection and the results are reasonably representative in other respects.

III. CONCLUSIONS

Black-Si was produced on Si surfaces by reactive ion etching with different needle heights from 0.2 to 4 μm. Controlling the process conditions allows b-Si to be obtained with low reflectivity and high carrier generation efficiency in the underlying Si, providing a simple means of producing an antireflection coating on Si. Metalization of b-Si and modification of the needle length allows either high or ultra low 0.04% reflectivity to be obtained. The low reflectivity material is promising for thermal sensor applications[4].

Differential reflectivity decay measurements were used for a contactless characterization of the b-Si photoelectronic properties and revealed the effects of the surface modification under various environmental conditions. Optimized b-Si production conditions allow very low $\sim$ 100 cm/s surface recombination velocities on b-Si needles, which are critical for effective photovoltaic device operation. For modeling of optical properties and experimental response, a combination of the

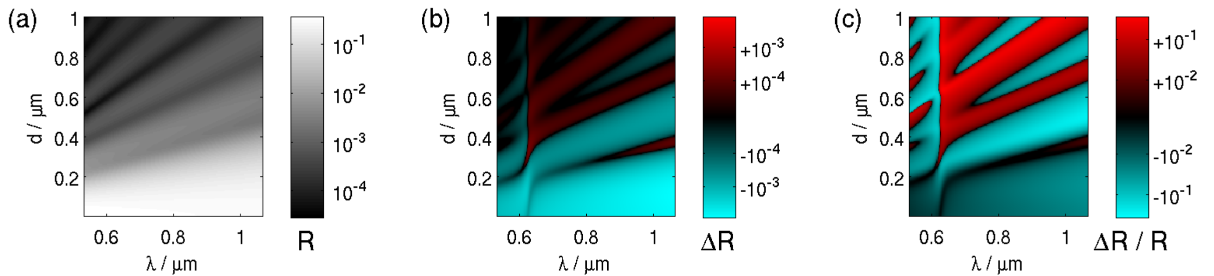

FIG. 5: Estimated differential reflection for a graded black Si layer (with linear conical profile) of varying thickness d, showing (a) unperturbed reflectance, (b) change in reflectance, and (c) relative reflectance change. Color represents the sign of the change (red higher, cyan lower). The calculation was performed using 532 nm pump and probe wavelengths as shown, for p-type 0.001 Ω.cm Si. All of the higher resistivity results are similar, assuming that the backside reflection is not collected.

augmented Drude excited-carriers and graded effective-medium models were employed. The revealed dependence of the differential reflectivity on probe wavelength (0.1 to 1 μm) and needle parameters (length in 0.5-1.1 μm range) has provided insights into tailoring the b-Si properties for sensor applications, based on refractive index modulation in the vicinity of the strong reflectivity dip.

The experimentally observed reflectivity of b-Si increased linearly with excitation intensity for pyramidal needles ($\Delta R > 0$), while it decreased for Si ($\Delta R < 0$), indicating excitation independent absorption. Also, some of the b-Si surfaces showed very low reflectivity of ∼0.01%. Both of these properties can potentially be useful for designing sensors and engineering light harvesting systems.

Experimental Section

Black-Si samples Samples of b-Si were made from a single-side polished p-type ⟨100⟩ orientation Si wafer (Atecom Ltd, Taiwan) with specific resistivity of 10 - 20 Ω.cm, unless otherwise specified. Plasma dry etching for nano-texturing the Si surface was carried out in a flow of mixed SF_6:O_2 at controlled bias (dry reactive ion plasma etching - DRIE) and voltage of the inductively-coupled plasma (ICP). The interplay between RIE and ICP controls the surface etching anisotropy together with the chamber pressure.

Batch No. 1 was made on a RIE-101iPH (SAMCO Inc.) etching tool capable of performing RIE and ICP-assisted RIE experiments. The 150 W ICP and 15 W (RIE) bias powers were typically used at a gas flow of 35 sccm for SF_6 and 45 sccm for O_2. The chamber pressure was 1 Pa and etching time was 15 min. This resulted in pyramidally shaped pillars. This recipe was used for the majority of samples tested in the pump-probe experiments.

Batches No. 2 and 3 were fabricated in an Oxford PlasmaLab 100 ICP380 system, which allows a greater degree of structural control. Here the SF_6 gas flow rate was 65 sccm, O_2 gas flow rate 44 sccm, process pressure 35 mTorr, 100 W RIE power, 20 °C electrode temperature and 10 Torr He backside cooling pressure[5]. Nanopillars of aspect ratio up to 2.2 ± 0.3 were formed in ∼ 25 min over the full area of 3- and 4-inch wafers under these conditions.

Magnetron sputtering (AXXIS, Kurt J. Lesker Ltd) was used for Au and Pd deposition with a well-controlled thickness for scanning electron microscope (SEM) inspection as well as for pump-probe experiments. Thickness of coating corresponds to that on a flat substrate. Transmission electron microscopy (TEM) analysis was carried out on a Jeol 2100F microscope equipped with a energy dispersive spectrometer (EDS) for surface chemical analysis.

The separation between b-Si needles followed a diffusional dependence on the etching time $x(t) = x(t = 5\text{ min})\sqrt{t}$. For Batches No. 2 and 3 the average separation was 388 ± 20 nm and 842 ± 30 nm, respectively (Fig. 1). For Batch No. 1, the separation was ∼ 300 nm and the pillars had a pyramidal shape of height ∼ 500 nm, similar to Batch No. 2. Batches 1 and 2 had comparable pillar heights, but for Batch 3 the height was ∼ 4 μm as the etching time was longer. For etching times above 0.5 h strong pillar height disorder sets in, leading to short wavelength light scattering[11].

Ellipsometry measurements A Woollam V-Vase Ellipsometer was used to measure the ellipsometric reflection values of Ψ and Δ. To complement the ellipsometry measurements polarised angular dependent reflectance was also assessed using a Perkin Elmer Lambda 950 with a Universal Reflectance Accessory. Following this the measured data was fitted using a graded effective medium profile to model the geometrical profile of the random pyramidal structures via a spectrally wide best fit. The thickness of the oxide layer was also used as a fit parameter. Standard multilayer thin film calculations based on a graded effective medium[28] were used for the needles. As the ellipsometry measurement is specular in nature, the backside reflectance of the Si wafer was neglected for the ellipsometric analysis (as the backside was un-polished). The collected data was fitted using the

Woollam WVASE software with the optical model in order to estimate the refractive index and Si concentration profile through the thickness of the b-Si layer. Starting b-Si profile values were based on the SEM profile, i.e. needles on top of pyramids (Fig. 1). In addition to Si and void, a native silicon dioxide component was included to achieve a better fit. The profile parameters were allowed to vary until a good fit to experimental data was obtained (Batch No.1). The fit was relatively poor below 0.5 μm, which is expected because of scattering due to the feature size being comparable to the wavelength of light.

Pump-probe measurements Photo-excitation (pump) of the samples in reflectivity $DR \equiv \Delta R/R$ and transmittivity $DT \equiv \Delta T/T$ measurements was performed by 15 ps duration laser pulses at 532 nm wavelength. The excitation intensity was varied from $I_0 \approx 0.1$ mJ/cm^2 to ~ 5 mJ/cm^2, which generated an excess carrier (electron-hole pairs) density at the excited surface $\Delta N_0 = \alpha_{ex} I_0 / h\nu_{ex}$ in a range from $\sim 10^{18}$ cm^{-3} up to $\sim 10^{20}$ cm^{-3}. The photoexcited carriers were distributed within a layer of thickness $d_{ex} = 1/\alpha_{ex} \sim 1$ μm. Here $h\nu_{ex} = 2.33$ eV is the photon energy at the excitation wavelength and the absorption coefficient[15] $\alpha_{ex} \simeq 10^4$ cm^{-1}.

An optically delayed (up to 4 ns) 25 ps duration probe beam at $\lambda_{pr} = 1064$ nm wavelength ($h\nu_{pr} = 1.18$ eV) was used to monitor the fast decay transients of the induced differential reflectivity (DR) and transmittivity (DT) decay kinetics. For reflectivity and transmittivity detection at 1064 nm, filters with a blocking ratio of 10^{-6} were used to block the 532 nm excitation radiation (note that the excitation and probe paths were also different to exclude excitation radiation at the probe detectors).

Pump-probe model calculations The pump-probe response shown in Fig. 5 was estimated using a combination of an augmented Drude excited-carrier model and a graded effective-medium model similar to that employed in the ellipsometry. The material model assumed that the absorption of pump photons (at 532 nm) is proportional to the product of the optical intensity and the imaginary part of the refractive index and that all photons absorbed in the silicon were converted into carriers. Separate Drude terms were used with electron and hole mobilities based on a known unpumped impurity concentration[15]. It was determined that a graded doping profile would not be important in most cases. A transfer-matrix thin-film model was employed, with 100 layers sampling the graded profile. A linear conical structure was simulated as a quadratic change in Si concentration (0 at cover and 1 at substrate) in a vertically oriented uniaxial Bruggeman effective-medium model, with zero vertical depolarization. Other profiles were tested but the linear profile is the simplest assumption that is consistent with experimental micrographs. The intensity-dependent refractive-index profile was made self-consistent with the optical intensity profile, although this coupling was found to be unimportant in most cases. Backside reflection would contribute to scattering from the sample at the resistivities used in the experiment, but was omitted due to the experimental geometry that excluded diffuse reflectance contributions, and as confirmed by the linear pump-power dependence.

Acknowledgements

PŠ acknowledges support from Lithuanian Academy of Science via the Young Scientists Scholarship. SJ is grateful for support by ARC Discovery DP130101205 grant. IA is the recipient of an Australian Research Council Discovery Early Career Research Award (Project No. DE130100592). AG and MA are grateful for support by ARC Discovery DP140102003 grant.

---

* Electronic address: `Patrik.Scajev@ff.vu.lt`
† Electronic address: `SJuodkazis@swin.edu.au`

[1] E. P. Ivanova, J. Hasan, H. K. Webb, G. Gervinskas, S. Juodkazis, V. K. Truong, A. H. F. Wu, R. N. Lamb, V. Baulin, G. S. Watson, J. A. Watson, D. E. Mainwaring, and R. J. Crawford, "Bactericidal activity of nanostructured black silicon," *Nature Commun.* **4**, 2838, 2013.
[2] G. Gervinskas, G. Seniutinas, J. S. Hartley, S. Kandasamy, P. R. Stoddart, and S. Juodkazis, "Surface-enhanced Raman scattering sensing on black silicon," *Annalen der Physik* **525**(12), 907 – 914, 2013.
[3] G. Seniutinas, G. Gervinskas, R. Verma, B. D. Gupta, F. Lapierre, P. R. Stoddart, F. Clark, S. L. McArthur, and S. Juodkazis, "Versatile SERS sensing based on black silicon," *Optics Express* **23**(5), 6763 – 6772, 2015.
[4] R. Komatsu, A. Balčytis, G. Seniutinas, T. Yamamura, Y. Nishijima, and S. Juodkazis, "Plasmonic photo-thermoelectric energy converter with black-Si absorber," *Solar Energy Materials Solar Cells* **143**, 72 – 77, 2015.
[5] A. Žukauskas, M. Malinauskas, A. Kadys, G. Gervinskas, G. Seniutinas, S. Kandasamy, and S. Juodkazis, "Black silicon: substrate for laser 3D micro/nano-polymerization," *Optics Express* **21**(6), 6901–6909, 2013.
[6] J. Oh, H.-C. Yuan, and H. M. Branz, "An 18.2 % efficient black-silicon solar cell achieved through control of carrier recombination in nanostructures," *Nature Nanotechn.* **7**, 743–748, 2012.
[7] K.-C. Park, H. J. Choi, C.-H. Chang, R. E. Cohen, G. H. McKinley, and G. Barbastathis, "Nanotextured silica surfaces with robust superhydrophobicity and omnidirectional broadband supertransmissivity," *ACS Nano* **5**(5), 3789–3799, 2012.
[8] P. R. Stoddart, P. J. Cadusch, T. M. Boyce, R. M. Erasmus, and J. D. Comins, "Optical properties of chitin: surface-enhanced raman scattering substrates based on antireflection structures on cicada wings," *Nanotechnol-*

ogy **17**, 680–686, 2006.

[9] K. Juodkazis, J. Juodkazytė, B. Šebeka, I. Savickaja, and S. Juodkazis, "Photoelectrochemistry of silicon in HF solution," *J. Solid State Electrochem.* **17**(8), 2269–2276, 2013.

[10] S. Eyderman, S. John, and A. Deinega, "Solar light trapping in slanted conical-pore photonic crystals: Beyond statistical ray trapping," *J. Appl. Phys.* **113**, 154315, 2013.

[11] G. Gervinskas, G. Seniutinas, J. S. Hartley, S. Kandasamy, P. R. Stoddart, N. F. Fahim, and S. Juodkazis, "Surface-enhanced Raman scattering sensing on black silicon," *Annalen der Physik* **525**(12), 907–914, 2013.

[12] A. J. Sabbah and D. M. Riffe, "Femtosecond pump-probe reflectivity study of silicon carrier dynamics," *Phys. Rev. B* **66**, 165217, 2002.

[13] G. Vuye, S. Fisson, V. Nguyen Van, Y. Wang, J. Rivory and F. Abelés, "Temperature dependence of the dielectric function of silicon using in situ spectroscopic ellipsometry," *Thin Solid Films* **233**, 166-170, 1993.

[14] P. Ščajev, "Application of excite-probe techniques for determination of surface, bulk and nonlinear recombination rates in cubic SiC," *Mater. Sci. Eng. B* **185**, 37–44, 2014.

[15] S. M. Sze, *Physics of Semiconductor Devices*, John Wiley and Sons, New York, 1981.

[16] M. Cardona and F. H. Pollak, "Energy-band structure of germanium and silicon," *Phys. Rev. B* **142**, 530–543, 1966.

[17] B. J. Frey, D. B. Leviton, and T. J. Madison, "Temperature-dependent refractive index of silicon and germanium," in *Optomechanical Technologies for Astronomy*, E. Atad-Ettedgui, J. Antebi, and D. Lemke, eds., p. 62732J, Proc. SPIE vol. 6273, 2006.

[18] P. Ščajev and K. Jarašiūnas, "Application of a time-resolved four-wave mixing technique for the determination of thermal properties of 4H-SiC crystals," *J. Phys. D: Appl. Phys.* **42**, 055413, 2009.

[19] P. Flubacher, A. J. Leadbetter, and J. A. Morrison, "The heat capacity of pure silicon and germanium and properties of their vibrational frequency spectra," *Phil. Mag.* **4**(39), 273–294, 1959.

[20] J. Linnros, "Carrier lifetime measurements using free carrier absorption transients. i. principle and injection dependence," *J. Appl. Phys.* **84**, 275–283, 1998.

[21] C. Klingshirn, *Semiconductor Optics*, Springer-Verlag, Berlin, 2nd ed., 2005.

[22] P. Grivickas, *Optical Studies of Carrier Transport and Fundamental Absorption in 4H-SiC and Si.* PhD thesis, Royal Institute of Technology, Sweeden, 2004.

[23] P. Ščajev, A. Usikov, V. Soukhoveev, R. Aleksiejūnas, and K. Jarašiūnas, "Diffusion-limited nonradiative recombination at extended defects in hydride vapor phase epitaxy GaN layers," *Appl. Phys. Lett.* **98**, 202105, 2011.

[24] S. Glunz, R. Preu, and D. Biro, *Comprehensive Renewable Energy*, vol. 1, ch. Crystalline Silicon Solar Cells - State-of-the-Art and Future Developments. Elsevier, 2012.

[25] S. Kumar, P. K. Singh, G. S. Chilana, and S. R. Dhariwal, "Generation and recombination lifetime measurement in silicon wafers using impedance spectroscopy," *Semicond. Sci. Technol.* **24**, 095001, 2009.

[26] R. D. Westbrook, *Lifetime Factors in Silicon*, Baltimore, 1980.

[27] J. Dziewior and W. Schmid, "Auger coefficients for highly doped and highly excited silicon," *Appl. Phys. Lett.* **31**, 346–348, 1977.

[28] P. G. Snyder, Y. M. Xiong, J. A. Woollam, G. A. A. Jumaily, and F. J. Gagliardi, "Graded refractive index silicon oxynitride thin film characterized by spectroscopic ellipsometry,," *J. Vac. Sci. Technol.* **A10**, 1462, 1992.